Geoscience Frontiers 14 (2023) 101677

Contents lists available at ScienceDirect

Geoscience Frontiers

journal homepage: www.elsevier.com/locate/gsf

Research Paper

Shale oil resource evaluation with an improved understanding of free hydrocarbons: Insights from three-step hydrocarbon thermal desorption

Gang Yan [a,b], Yao-Hui Xu [b,*], Wang-Lin Xu [c], Bin Bai [c], Ying Bai [c], Yun-Peng Fan [b], Shan-Shan Li [b], Ming Zhong [d], Yan Liu [b], Zhi-Yao Xu [e]

[a] Cooperative Innovation Center of Unconventional Oil and Gas, Yangtze University (Ministry of Education & Hubei Province), Wuhan 430100, China
[b] Hubei Key Laboratory of Petroleum Geochemistry and Environment, Yangtze University, Wuhan 430100, China
[c] Research Institute of Petroleum Exploration and Development, PetroChina, Beijing 100083, China
[d] School of Energy and Resources, China University of Geosciences, Beijing 100083, China
[e] Suzhou Grand Energy Technology Co. Ltd, Suzhou 215129, China

ARTICLE INFO

Article history:
Received 20 October 2022
Revised 8 June 2023
Accepted 16 July 2023
Available online 20 July 2023
Handling Editor: Inna Safonova

Keywords:
Shale oil
Hydrocarbon thermal desorption
Resource evaluation
Component
Microscopic occurrence feature

ABSTRACT

The pyrolysis parameter S_1, which indicates the amount of free hydrocarbons present in shale, is often underestimated due to hydrocarbon loss during sample handling and measurement processes. To remedy this issue, we strongly recommend an immediate three-step hydrocarbon thermal desorption (HTD) approach to be conducted on oil shale at the drilling site. This approach measures S_g, S_0, and S_1*, which refer to gaseous, light, and free hydrocarbons, respectively. The new shale oil content value, calculated from the total of these three parameters, is far more precise and reliable than traditional pyrolysis S_1. Moreover, we thoroughly investigated the components and microscopic occurrence features of hydrocarbons thermally desorbed at three temperature stages using gas chromatography (GC) and X-ray micro-computed tomography (CT). For example, we selected Chang 7_3 mud shale. Our experimental results irrefutably indicate that the ultimate shale oil content of poor resource rocks is significantly impacted by evaporative loss, with this effect being greater when the total organic carbon (TOC) is lower. Additionally, $C_{1\text{-}5}$ and $C_{1\text{-}7}$ hydrocarbons constitute almost all of S_g and S_0, respectively. S_g and S_0 are predominantly composed of $C_{1\text{-}3}$ gaseous hydrocarbons, with a maximum proportion of 42.93%. In contrast, S_1* contains a substantial amount of $C_{16\text{-}31}$ hydrocarbons. A three-dimensional reconstruction model of an X-ray micro-CT scan shows that while the amount of shale organic matter greatly decreases from the frozen state to 300 °C, the pore volume significantly increases, particularly between 90 and 300 °C. The increased pore volume is mainly due to macropores and fractures. It is imperative to note that the shale oil triple-division boundaries must be adjusted based on more accurate oil content, although this would not affect the resource zones to which the samples already belong (ineffective, low-efficient, and enriched resources). In conclusion, we strongly advise conducting an immediate well-site analysis or utilizing preservation procedures, such as deep freezing or plastic film wrapping followed by core waxing, to minimize volatile loss.

1. Introduction

The future of fossil fuel resources lies in unconventional hydrocarbons, and the most attractive unconventional reserves are shale gas and oil (Wright et al., 2015). Chinese lacustrine shale oil varies significantly from North American shale oil in terms of sedimentary characteristics (Pu et al., 2016); (Sun et al., 2019); (Zhao et al., 2019); mechanism for generation and accumulation (Zhu et al., 2019); (Kuang et al., 2022); and fluid parameters (Sun et al., 2019). However, fractured shale oil has been found in numerous basins since the 1970 s, including the Ordos, Junggar, Bohai Bay, Songliao, Qaidam, and Jianghan Basins (Li et al., 2015; Wang et al., 2015; Yang et al., 2016; Hou et al., 2017; Liu et al., 2017; Zhang et al., 2017; Chen et al., 2018; Tang et al., 2021). The United States Energy Information Administration (EIA, 2015) reports that China has an estimated 4.37 billion tons of shale oil resources that can be technically recovered. And the China National Energy Administration predicted national recoverable shale oil resources ranging from 7.4 to 37.2 billion tons (Jin et al., 2019). Successfully

* Corresponding author.
E-mail address: yaohuixu@126.com (Y.-H. Xu).

https://doi.org/10.1016/j.gsf.2023.101677

addressing certain technological and theoretical obstacles is imperative if China's continental shale oil is to serve as a viable substitute for petroleum reserves and effectively bolster fossil fuel production.

Determining the oil content is crucial in identifying potential intervals for exploration and development in lacustrine shale oil systems. It also plays a significant role in the study of the primary factors that influence the differential accumulation of shale oil (Liu et al., 2021). One parameter that's commonly used is the free oil content (S_1). This refers to the volatile hydrocarbon fraction that's either free or residual in the rock after hydrocarbon generation. In order to determine the S_1, a Rock-Eval pyrolysis of shale is typically performed. This process identifies the hydrocarbons (C_7-C_{33}) that would be volatilized at temperatures below 300℃ (Jarvie, 2012); Wang, 2022b). However, it's often underestimated due to the loss of light hydrocarbons during measurement. Sample preparation and analysis delay could result in up to 60% reduction in the Rock–Eval S_1 peaks for the preserved shale cores (Li et al., 2022). This means that shale oil resources may be underestimated by 2–3 times before correcting for this loss(Jarvie et al., 2007); (Bohacs et al., 2013). Factors like core storage conditions, experimental testing analysis, and kerogen adsorption can affect the loss of these hydrocarbons (Hunt et al., 1980); (Cooles et al., 1986); (Wang et al., 2014). In some cases, estimates of original oil-in-place based on S_1 values from traditional Rock-Eval analyses on poorly maintained samples could significantly underestimate the prospective resource yield of target plays (Jiang et al., 2016). Therefore, more research is needed to determine shale oil content experimentally and study the effects of various parameters (Wang et al., 2022).

It has been conclusively demonstrated that the duration for which source rocks are preserved has a direct impact on the loss of light hydrocarbons(Zhang et al., 2012). And the significant evaporative loss of gaseous and light hydrocarbons (up to C_{10}) can occur during the collection, storage, and laboratory preparation stages(Li et al., 2022). It is also concluded that the total organic carbon (TOC) in sedimentary rocks could be a crucial factor in the retention and preservation of light hydrocarbons (Jiang et al., 2016). However, restoring such losses in estimating shale oil resources and determining mobility is a widely recognized challenge. In the previous study, some more effective pyrolysis methods had been devised to determine the exact amount of oil(Jiang et al., 2016); (Li et al., 2019); (Romero-Sarmiento, 2019). Their improved technique involves a wider temperature range to eliminate heavy hydrocarbons that have high boiling points or that interact strongly with the rock matrix. Moreover, Wang et al. (Wang et al., 2014) calculated the correction factors and established a model of light hydrocarbon loss and heavy hydrocarbon handling on the base of pyrolysis experiments and kinetic models of hydrocarbon generation. Scholars have established a connection between the loss of light hydrocarbons (C15-) and oil API gravity by examining core-extracted oils instead of core-produced oils. This relationship is then utilized by other researchers to estimate shale oil resources (Abrams et al., 2014). A new method called the oil content evaluation index (OCEI) was created by Liu et al. (2021) that takes into account the shale oil composition to assess the vertical distribution of oil content using conventional logging. While various methods exist, they often include multiple indicators and can be difficult to use, limiting their usefulness for guiding shale oil exploration and development.

Shale of the Chang 7 Member in Yanchang Formation, Ordos Basin shows excellent potential for shale oil exploration prospects (Zhang et al., 2017); (Wang et al., 2019), and it is essential to perform accurate and rapid shale oil content evaluations. In this work, by combining the technologies of sampling at the drilling site and closed crushing in the frozen state, we performed hydrocarbon thermal desorption (HTD) experiments on the lower mud shale of the Chang 7 member (Chang 7_3 submember) at the drilling site of Well LY-10 to obtain the shale oil content quickly and accurately. This innovative and rapid method can minimize the loss of light hydrocarbons during sample storage, transportation, and crushing. Additionally, by combining gas chromatography (GC) and X-ray microcomputed tomography (CT), we analyzed the components and microscopic occurrence characteristics of hydrocarbons thermally desorbed at different temperatures. This work will provide an innovative method for the rapid and accurate evaluation of shale oil content and offer theoretical support for shale oil exploration.

2. Geological settings

Lacustrine shales in China occupy an area of approximately 280,000 square kilometers (Wang et al., 2019), and the Ordos Basin is located west of the North China Platform (Fig. 1a). This basin is a large multi-cycle cratonic basin, which is bound to the east by the Lvliang Mountain and Lishi Fault, to the west by the Helan Mountain, to the north by the Xing'an Mongolian Orogenic Belt and the Dengkou-tuoketuo Fault, and to the south by the Qinling Orogenic Belt and Huaibei Flexure Belt(Yang et al., 2007); (Lin et al., 2023). It experienced major interior changes during the Late Triassic period, and a large-scale inland-depression lake basin formed affected by the Indosinian Orogeny (Fu et al., 2020). Within the basin, a sequence of river–delta–lacustrine strata belonging to the Upper Triassic Yanchang Formation were deposited. These strata were split into ten components from top to bottom (Chang 1–10). The Chang 7 member was deposited at the most flood-prone time, resulting in a large deposit of freshwater organic-rich shale with a wide distribution range in the component; thus, Chang 7 is the main source rock in the Ordos Basin's Mesozoic epoch (Yang and Zhang, 2005); (Yang et al., 2016). The Chang 7 members may be generally separated into three submembers, namely, the Chang 7_1, Chang 7_2, and Chang 7_3 submember (Yang et al., 2016). The observed thinly-bedded sandstones of gravity flow origin and the thickly-bedded shales mainly deposited in the deep-lake area(Liu et al., 2021). According to the lithological description, the gravity flow sandstones mainly occur at the top and bottom of the Chang 7_3 submember, while the thickly-bedded shales are deposited between them (Lin et al., 2023). The thickly-bedded shales in the Chang 7_3 submember were deposited during the Carnian Pluvial Event (CPE) in the late Triassic (Preto et al., 2010); (Corso et al., 2018). The Ordos Basin is separated into six structural units by tectonic plates: the Yimeng Uplift, Weibei Uplift, Jinxi Folding Belt, Yishan Slope, Tianhuan Depression, and Western Edge Thrust Belt (Liu et al., 2021). Over 90% of the oil fields in the Ordos Basin have been discovered on the Yishan Slope, and the LY-10 Well in this study is likewise located on the Yishan Slope (Fig. 1a).

3. Samples and experimental methods

3.1. Samples

The majority of the samples selected for this investigation were taken from the Chang 7_3 sub-member of Well LY-10. These samples were predominantly charcoal-gray or grayish-black mudstone and grayish-black carbonaceous mudstone, with a very small percentage of gray argillaceous siltstone (Fig. 1b). To avoid the loss of gaseous and light hydrocarbons, 82 samples were immediately wrapped in plastic wrap and held in a −20 °C refrigerator after excavation. At the well site, the HTD tests were performed on a total of 49 samples. Additionally, an air collection bag and dichloromethane-containing bottles were used for collecting

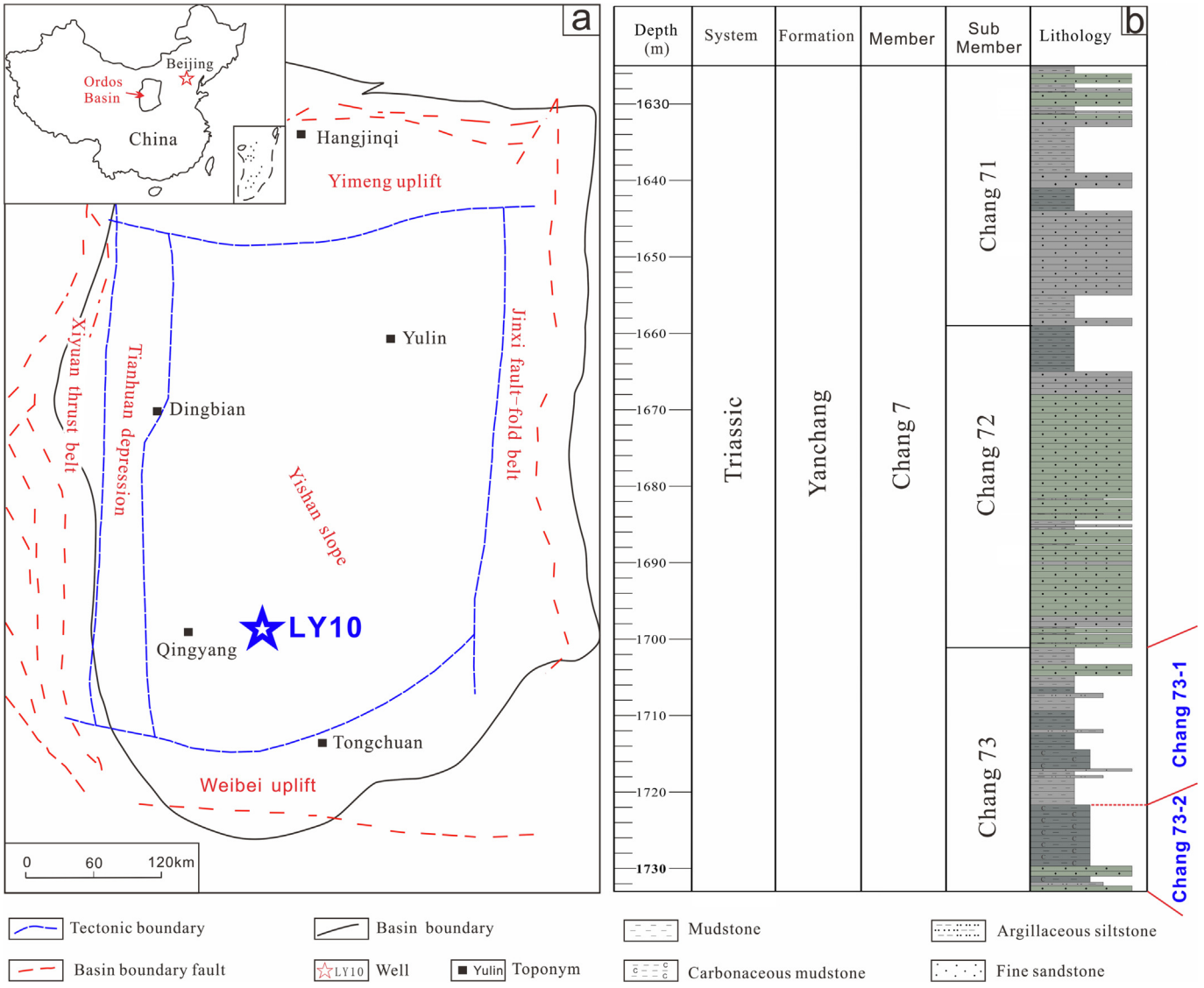

Fig. 1. Structural units of the Ordos Basin (modified from Liu et al., 2021), showing (a) the location of Well LY-10 in the Ordos Basin and (b) the stratigraphic column in the study area.

hydrocarbons from two selected carbonaceous mudstone samples (S_{74} and S_{79}). In addition, several analyses, including TOC content, Rock-Eval pyrolysis, vitrinite reflectance (R_o) measurements, GC, and X-ray micro-CT, were all performed in the laboratory.

3.2. TOC analysis

The TOC content was measured with a LECO CS230 carbon and sulfur analyzer, and its accuracy was within 0.03%. The crushed samples (200 mesh) were first immersed in a 12.5% HCl solution for 24 h to eliminate all inorganic carbonate minerals. Then, the powder samples were rinsed several times with deionized water to fully remove the HCl. Finally, they were dried at 80 °C in an oven for 24 h, and the TOC values were obtained through combustion.

3.3. Vitrinite reflectance (R_o) and organic maceral measurements

To evaluate the thermal maturity and organic matter types of source rocks, 15 samples at different depths were selected to measure the R_o and to observe the organic maceral compositions. The experiments were conducted with an instrument that combined the Zeiss Axio Scope.A1 Microscope and Tidas J&M Msp 200 systems. The sample was crushed to 20–40 mesh particle sizes and formed into the desired shape with epoxy resin during processing. The samples were ground smoothly with different grit sandpapers and polished with a polishing solution. The R_o values were calculated by the double-labeling method, and they were found to be 0.589% and 1.717% for the two specimens, respectively. The organic maceral measurements were taken by a Zeiss Axio Scope.A1 Microscope with reflected white light and fluorescence light.

3.4. Rock-Eval pyrolysis and hydrocarbon thermal desorption experiments

The conventional programmed Rock-Eval pyrolysis was performed with the OGE-VI pyroanalyzer designed by the Institute of Petroleum Exploration and Development, CNPC. The rock samples were first crushed to 100 mesh particle sizes, and then approximately 100 mg powders were selected to perform programmed pyrolysis to obtain the free oil content parameter S_1 and the pyrolysis hydrocarbon content S_2.

Meanwhile, the HTD experiments were conducted at the oilfield drilling site with a shale oil content analysis instrument made by Suzhou Grand Energy Technology Co. Ltd. (China). Once the rock samples were extracted from the well, approximately 1 g of each sample was selected and crushed directly with a special cryogenic sealed jar; from there, the sample was moved directly to the testing system to measure the oil content parameters.

3.5. TCD/FID-GC analysis

To characterize the carbon number distribution range, the thermally desorbed hydrocarbons collected at different temperature ranges were detected by an Agilent 7890A FID-GC equipped with an HP-PONA methylsiloxane column (50 m × 200 μm × 0.5 μm). Helium served as the carrier gas, and the constant flow rate of injection was 1 mL/min. The injection was performed manually, and the splitless mode was chosen. The GC oven temperature was initially held at 33 °C for 10 min, then increased to 63 °C at a rate of 3 °C/min; from there the temperature was increased to 325 °C at a rate of 6 °C/min and held for 25 min. Compound identification was performed by comparing the measured GC retention time and mass spectra with those found in the literature.

Simultaneously, the quantification of each component ($C_{1\text{-}5}$) in gaseous hydrocarbons (S_g and S_0) was performed on an Agilent 7890B GC equipped with a thermal conductivity detector (TCD). The capillary column used for analysis was a PoraPLOTQ column (20 m × 250 μm × 8 μm). The carrier gas and injection modes were the same as those used for FID-GC analysis. The volume of each manual injection was 200 μL of gaseous hydrocarbons. The GC oven temperature was initially held at 40 °C for 2 min, then increased to 100 °C at 15 °C/min and held for 5 min. The quantitation was calculated with the peak areas of the standard gas mixture compounds and the target HC compounds. The standard gas mixture was purchased from Foshan Kodi Gas Chemical Co., Ltd. (China), and the compositions are listed in Table 1.

3.6. X-ray Micro-CT

In this work, the X-ray micro-CT experiment was conducted at the State Key Laboratory of Petroleum Resources and Prospecting, China University of Petroleum (Beijing) with a high-resolution X-ray multiscale core scanning and imaging system (nanoVoxel-3502E, Sanying Precision Instruments Co., Ltd, China). The diameter of the core plug used in this experiment was 3 mm, corresponding to a CT scan image resolution reaching 3 μm. To characterize the changes in the occurrence state of shale oil during the HTD experiments, X-ray micro-CT experiments were performed on frozen samples and plugs heated to 90 °C and 300 °C in turn. From sample S_{79}, a 3-mm-diameter column was drilled and marked with a pencil to ensure consistency in the three subsequent scans. The first CT scan was conducted immediately after the successful drilling of the frozen sample. For the second scan, the column was heated in an oven at 90 °C for 24 h and cooled to room temperature. The third and final scan was done after heating the column at 300 °C for 24 h. The images from the resulting shale column CT scans were imported separately into the 3D visualization software AvizoFire 9.0. Each image was filtered to eliminate noise before the spatial distribution features of each component were segmented and reconstructed in 3D. We accounted for the differences in gray values among pores, organic matter, and rock particles. Lastly, we determined the volume distribution characteristics of the pores and organic matter.

4. Results

4.1. Source rock characteristics

4.1.1. Organic matter abundance

The lithology of the Chang 7_3 submember varied significantly vertically, as depicted in Fig. 1b and 2a. We classified it into two layers, namely Chang $7_{3\text{-}1}$ and Chang $7_{3\text{-}2}$. Mudstone was the predominant lithology in the Chang $7_{3\text{-}1}$ layer, with TOC content ranging from 0.50 to 26.30 wt%, averaging at 2.74 wt%. However, most of the samples had a TOC content below 4.00 wt% (Fig. 2b). In contrast, the Chang $7_{3\text{-}2}$ layer had a different lithology, mainly carbonaceous mudstone, and relatively high TOC content. The TOC content ranged from 3.85 to 41.86 wt%, averaging at 18.55 wt% with most samples having TOC content greater than 8.00 wt% (Fig. 2c). Therefore, the samples from the Chang $7_{3\text{-}2}$ layer were premium-quality source rocks.

4.1.2. Organic matter types and maturity

The graph depicting HI vs. Tmax indicates that the source rocks of Chang 7_3 submember were predominantly of type I-II_1 kerogen, with a significant amount of convertible organic carbon present (Fig. 3a). Fig. 3b displays the results of *Ro* values of the Chang 7 member source rocks. All of the samples analyzed were found to be thermally mature within the oil window, with *Ro* values ranging from 0.70% to 1.00%. These findings were further backed up by the Tmax values, which ranged from 441 °C to 450 °C (Fig. 3a and Supplementary Data Table S1), and primarily fell within the 430–450 °C range, signifying the oil window (Wang et al., 2022).

4.1.3. Maceral compositions of organic matter

According to Xie et al. (Xie et al., 2020), Lamalginite has a higher potential for generating hydrocarbons compared to other maceral compositions. The samples studied mostly consisted of alginites, solid bitumen, framboidal pyrite, and mineral-bituminous groundmass (Fig. 4), with alginites being the major organic component found in marine oil shales worldwide(Pickel et al., 2017). In the Chang 7_3 submember shales, alginites existed as solitary or colony organisms and lamalginite was abundant, appearing as elongated layers of small lamellae lying parallel to the beddings. Although it was challenging to distinguish lamalginite from the surrounding matrix under reflected white light, its bright yellow fluorescence set it apart (Khan et al., 2020). Telalginite, which had the same fluorescence as lamalginite, also constituted a significant proportion of the organic components (Fig. 4f). As a result, the alginite-rich oil shale of the Chang 7_3 submember exhibited excellent potential for hydrocarbon generation.

4.2. The contents, components and microscopic occurrence features of thermally desorbed hydrocarbons

4.2.1. The contents of thermally desorbed hydrocarbons

In Figs. 2 and 5, it was noticed that the Chang $7_{3\text{-}2}$ layer shales with higher TOC contents had corresponding thermally desorbed hydrocarbon concentrations, which included S_g, S_0, and $S_1{}^*$. Sup-

Table 1
Compositions of the standard gas mixtures.

	N_2	CO_2	CH_4	C_2H_6	C_3H_8	iC_4	nC_4	iC_5	nC_5
Concentration (%)	12.400	1.510	82.445	2.060	0.753	0.209	0.208	0.210	0.205

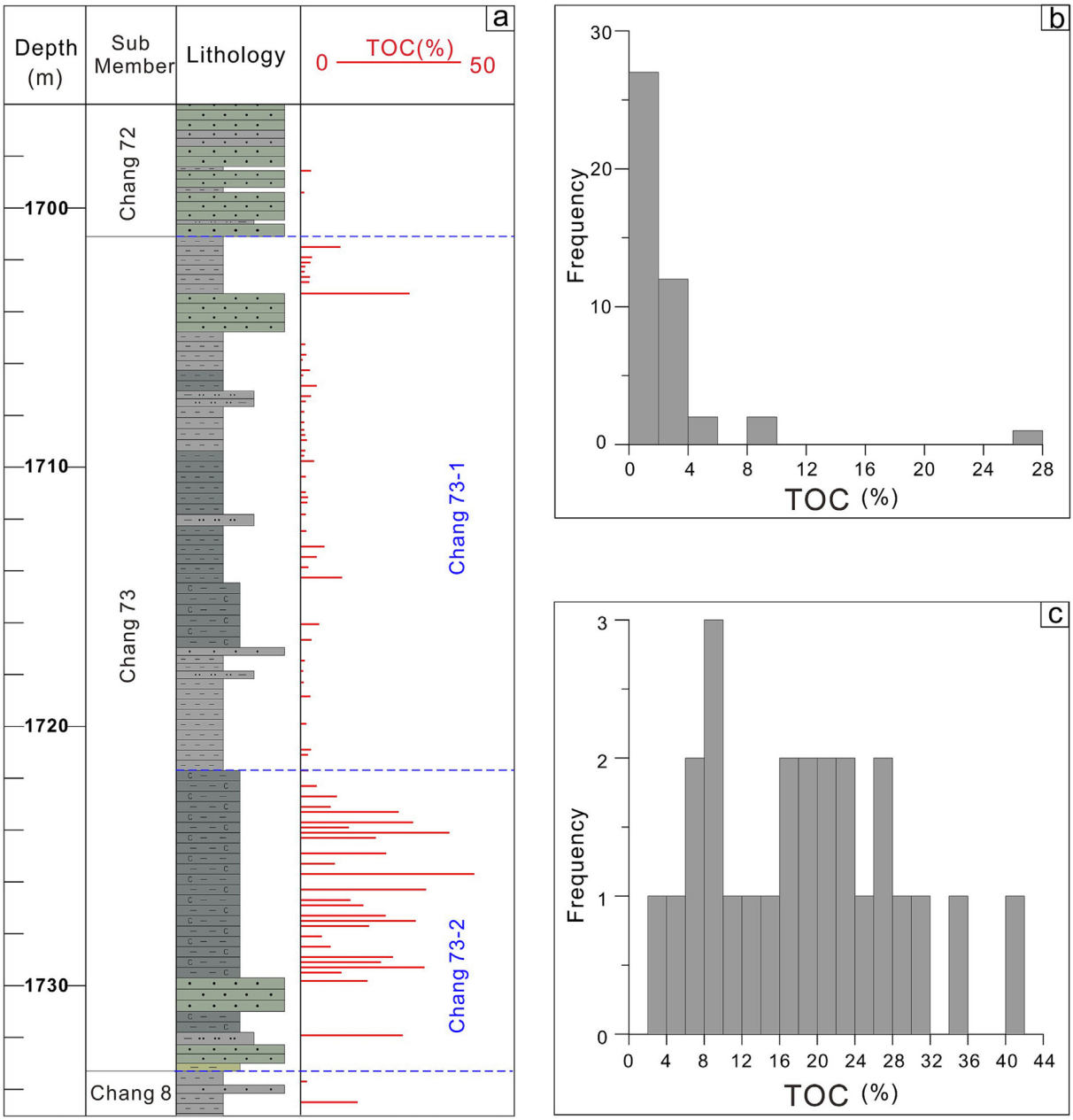

Fig. 2. TOC distribution of the Chang 7_3 submember source rocks. (a) Longitudinal distribution of TOC among the depths. (b) TOC statistics of the Chang $7_{3\text{-}1}$ layer. (c) TOC statistics of the Chang $7_{3\text{-}2}$ layer.

plementary Data Table S1 provides more details on the hydrocarbon content parameters. The S_g, S_0, and S_1* parameters of the Chang $7_{3\text{-}2}$ layer shales ranged from 0.04 to 0.98, 0.27 to 4.63, and 1.19 to 19.77 mg/g rock with mean values of 0.51, 2.21, and 9.92 mg/g rock, respectively. The Chang $7_{3\text{-}1}$ shale, on the other hand, had lower parameters compared to the Chang $7_{3\text{-}2}$ shale. Its S_g, S_0, and S_1* parameter values ranged from 0.01 to 0.52, 0.07 to 1.75, and 0.14 to 3.35 mg/g rock with mean values of 0.16, 0.56, and 1.35 mg/g rock, respectively.

4.2.2. The components of thermally desorbed hydrocarbons

The GC-FID traces of three hydrocarbons - gaseous (S_g), light (S_0), and free (S_1*) - collected from a shale sample S_{79} HTD experiment are shown in Fig. 6. Upon comparison with previously published data (Jiang et al., 2015); Jiang et al., 2016; (Hou et al., 2021), the components of these hydrocarbons were identified. S_g was composed entirely of gaseous hydrocarbons ($C_{1\text{-}5}$) (Fig. 6a and b) while S_0 had a larger abundance of $C_{1\text{-}5}$ hydrocarbons and negligible amounts of $C_{6\text{-}7}$ hydrocarbons such as 2-methylpentane, methylcyclopentane, benzene, and methylcyclohexane (Fig. 6a and c). Additionally, high carbon number (>C_{17}) n-alkanes were detected in S_0 (Fig. 6c). The GC-FID traces of S_1* showed a relatively high concentration of only $C_{16\text{-}31}$ hydrocarbons (Fig. 6d).

We also measured the hydrocarbon compounds in S_g and S_0 using the peak areas of the GC-TCD traces. To determine the relative percentages of $C_{1\text{-}5}$ gaseous hydrocarbons, we compared the experimental values to the percentages of each component in the standard gas mixture listed in Table 1. Table 2 and Fig. 7 show the relative abundances of $C_{1\text{-}5}$ gaseous hydrocarbons in both S_g and S_0 for two selected samples (S_{74} and S_{79}). $C_{1\text{-}3}$ gaseous hydrocarbons were prominent in both S_g and S_0, with C_3 in the S_0 of sample S_{74} accounting for the highest percentage of 42.93%. Ethane (C_2)

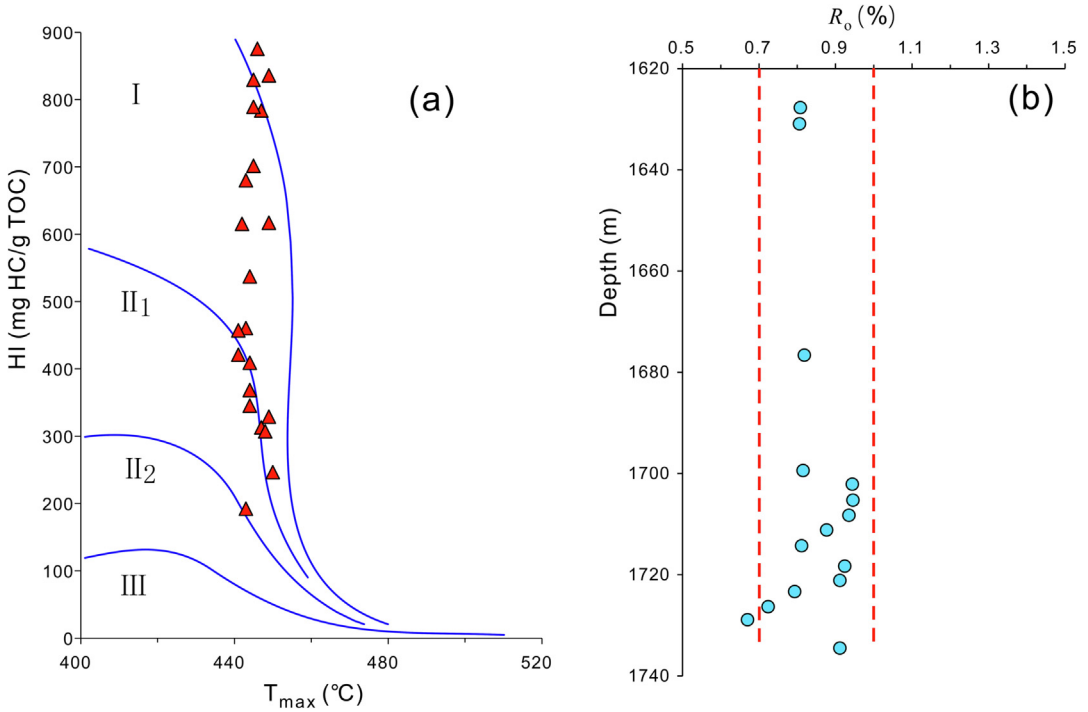

Fig. 3. (a) Source rock organic matter type evaluation and (b) thermal maturity of Chang 7 member source rocks.

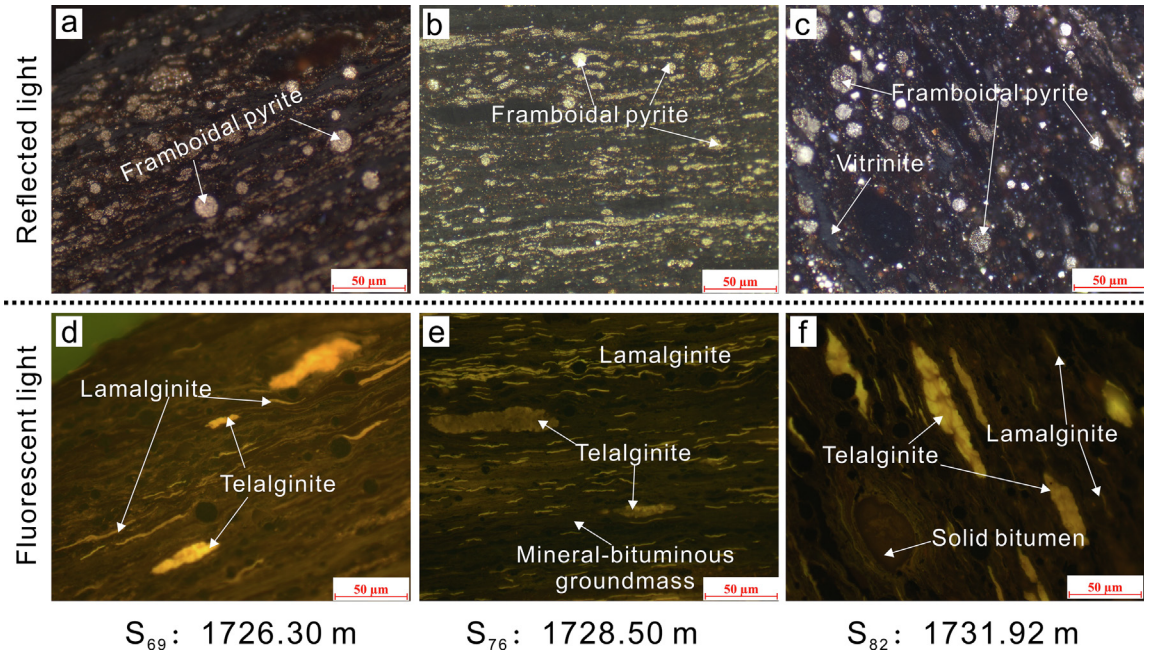

Fig. 4. Photomicrographs showing organic matter under reflected light (a, b, c) and fluorescent light (d, e, f). (a, d- S_{69}, 1726.30 m; b, e-S_{76}, 1728.50 m; and c, f-S_{82}, 1731.92 m).

and propane (C_3) were the most significant hydrocarbons in S_g, accounting for over 30% of the hydrocarbons. The percentages of $C_{1\text{-}3}$ varied more dramatically in S_0 hydrocarbons, progressively rising, with propane (C_3) accounting for approximately 40% of the hydrocarbons. The sum percentage ranging from C_1 to C_3 hydrocarbons was almost always higher than 60%, with a maximum of 86.81% (S_g of sample S_{79}). Apart from n-butane, which had a relatively higher proportion, the percentages of the other three C_4 and C_5 hydrocarbons, namely isobutane, isopentane, and n-pentane, were quite lower than $C_{1\text{-}3}$.

4.2.3. Microscopic occurrence features of thermally desorbed hydrocarbons

The gray values of shale pores were generally the lowest, while organic matter had slightly higher values, and high-density minerals like pyrite had the highest values(Saif et al., 2016). In Fig. 8 (a_1, a_2 and a_3), areas with low gray values are dark, while those with high gray values are light. The oil shale studied showed clear bedding, with white areas indicating framboidal pyrite along the beddings, as seen in Fig. 4. The three-dimensional model of organic matter reconstruction (Fig. 8 a2, b2, and c2) and pores (Fig. 8 a3,

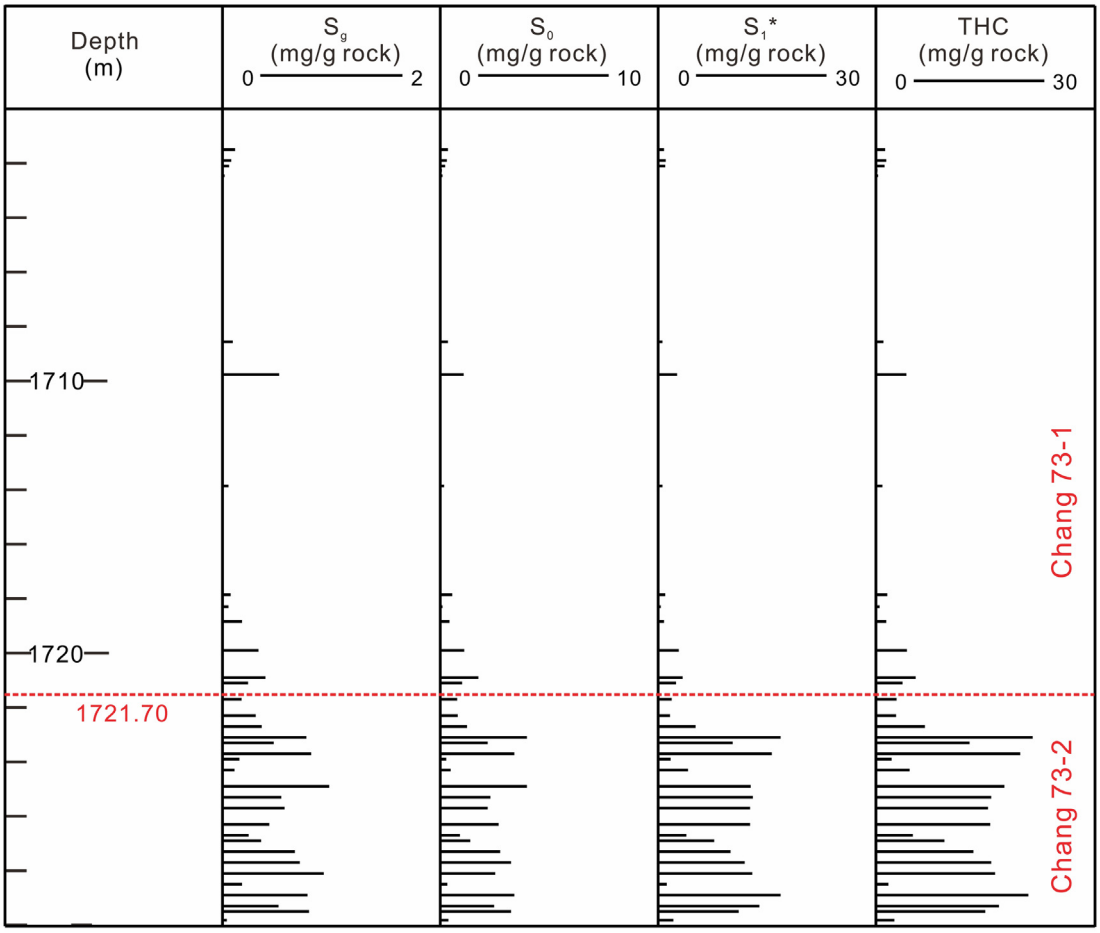

Fig. 5. Contents of hydrocarbons revealed by HTD experiments for Chang 7_3 submember shale. THC (mg / g rock) = S_g + S_0 + S_1*.

b3, and c3) showed that most of the organic matter filled the laminae. Heating at 90 °C led to a decrease in organic matter volume from 12.7% to 11.7%, while pore volume increased slightly from 0.49% to 0.65%. There was no noticeable change in either volume. The distribution of connected pores appeared to increase, while the volume of different connected pores represented by various colors seemed to vary little or even decrease, as seen in the red areas in Fig. 8 (a_3). However, heating at higher temperatures (300 °C) led to significant changes in both volumes. The organic matter volume decreased by 43.59% from 11.70 to 6.60%, while the pore volume increased by 69.23%, from 0.65 to 1.10%. Fig. 8 (c_3) showed a significant increase in both the number and volume of connected pores.

5. Discussions

5.1. Comparison between conventional Rock-Eval pyrolysis and hydrocarbon thermal desorption experiments

Figs. 9 and 10 illustrate the experimental procedures and FID pyrograms of traditional Rock-Eval pyrolysis and three-step hydrocarbon thermal desorption. In conventional Rock-Eval pyrolysis procedures, the sample is typically crushed to 100 mesh with an open mortar, and only 100 mg of rock powder is used for analysis, as shown in Fig. 9(a). Unfortunately, this process leads to the loss of most gaseous and light hydrocarbons, particularly those present in rock pores or adsorbed on mineral surfaces. Fig. 10a presents the FID pyrogram that indicates the evolution of organic compounds from rock samples during heating. The Rock-Eval pyrolysis parameter S_1 mainly indicates the free hydrocarbon content that is thermally desorbed when the system is rapidly heated to 300 °C (Peters, 1986). The pyrolysis S_2 parameter represents the content of kerogen-cracked hydrocarbons that appear as the system temperature increases to 600 °C at a rate of 25 °C/min in a helium environment. During this process, macromolecular organic matter and certain inorganic minerals in oil shale undergo thermal cracking and kerogen decomposition reactions to produce tar (Lei et al., 2021).

The three-step HTD experiment uses a device equipped with a flame ionization detector (FID), which is sensitive, has a wide range of linearity, and is stable for organic HC compounds (Budiman et al., 2015). By combining timely sampling and crushing samples in a closed grinding jar, gaseous and light hydrocarbons can be kept and detected as much as feasible (Fig. 9b). The sealed grinding jar is quickly moved to the low-temperature crusher for quick cooling, and the sample is only crushed when the temperature falls below 5 °C. Moreover, the grinding jar was completely sealed throughout the handling procedure, and make sure the temperature of the jar didn't increase during the crushing process. After finishing grinding, move the jar to the testing equipment. Then, connect the heating coil and carrier gas for FID testing. The HTD experiment consists of three steps: the low-temperature stage (less than5 °C), 5–90 °C, and 90–300 °C, from which the contents of free hydrocarbons in distinct occurrence states (S_g, S_0, and S_1*) can be derived (Fig. 10b). S_1* is similar to the conventional pyrolysis parameter S_1. The total hydrocarbon content (THC, mg.g-1 rock) is defined as the sum of S_g, S_0, and S_1* and is a more accurate and

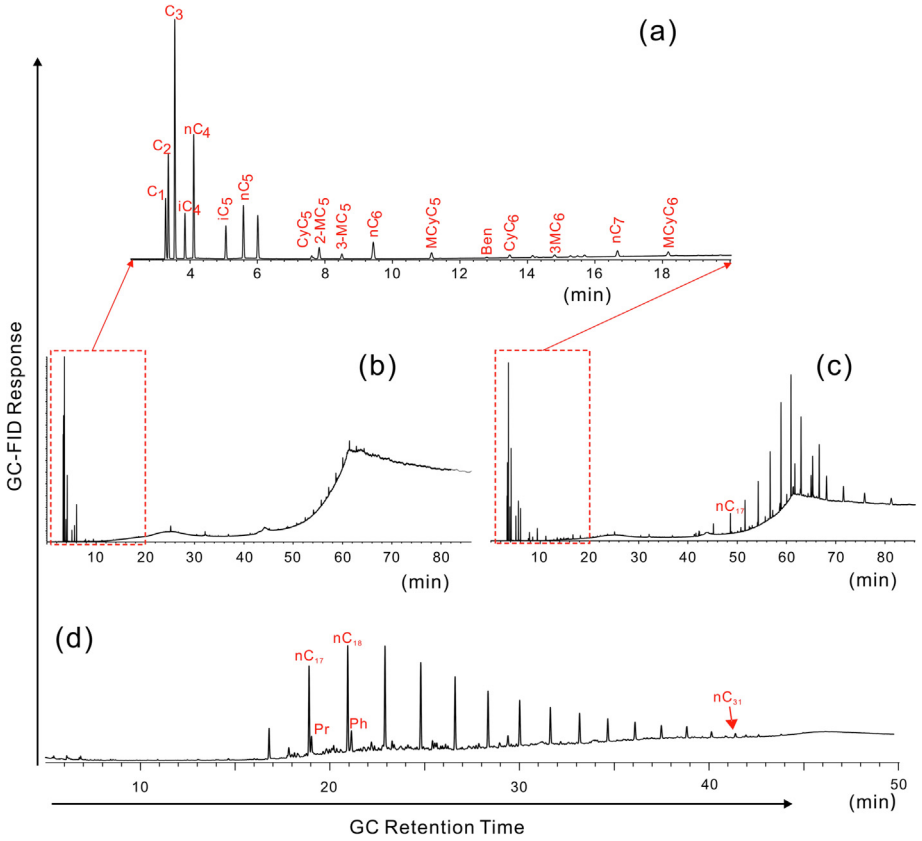

Fig. 6. HTD-GC-FID traces showing the compositions of hydrocarbons thermally desorbed from a Chang 7_3 shale core sample (S_{79}) at different temperature stages. (a) is an enlargement of the light hydrocarbon gas chromatogram. (b), (c), and (d) are the FID gas chromatograms of S_g, S_0 and S_1*, respectively. C_1: CH_4, methane; C_2: C_2H_6, ethane; C_3: C_3H_8, propane; iC_4: isobutane; nC_4: *n*-butane; iC_5: isopentane; nC_5: *n*-pentane; CyC_5: cyclopentane; 2-MC_5: 2-methyl pentane; 3-MC_5: 3-methyl pentane; $MCyC_5$: methyl cyclopentane; Ben: benzene; CyC_6: cyclohexane; 3-MC_6: 3-methyl hexane; $MCyC_6$: methyl cyclohexane; Pr: pristine; and Ph: phytane. Other labeled peaks denote the carbon numbers of the corresponding normal alkanes.

Table 2
Relative abundance of C_1, C_2, C_3, C_4, and C_5 gaseous hydrocarbons in both S_g and S_0 for two selected mud shales.

Sample ID	Relative abundance (%)								
		C_1	C_2	C_3	iC_4	nC_4	iC_5	nC_5	C_{1-3}
S_{74}	S_g	12.94	33.62	33.06	3.17	12.37	1.87	2.97	79.62
	S_0	9.31	17.86	42.93	4.32	15.61	3.47	6.50	70.10
S_{79}	S_g	22.91	31.19	32.71	1.40	8.92	1.17	1.70	86.81
	S_0	8.84	19.89	39.53	4.98	17.55	3.06	6.16	68.26

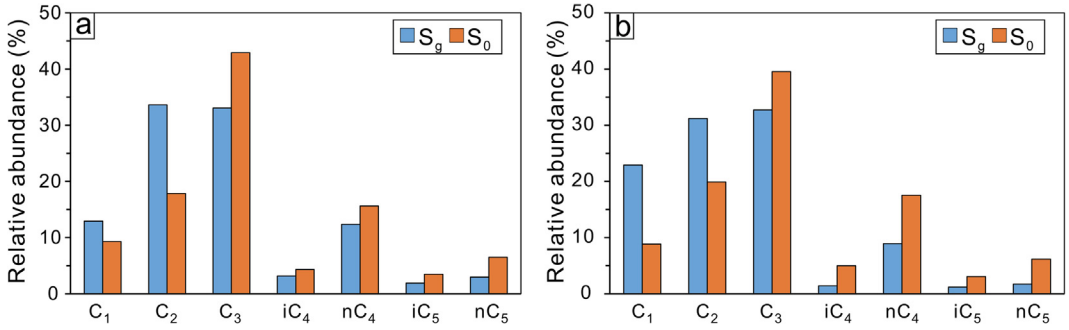

Fig. 7. The proportion of each component (from C_1 to C_5) in hydrocarbons S_g and S_0 for two Chang 7_3 shale core samples. (a): S_{74}, 1727.70 m; (b): S_{79}, 1729.30 m. C_1: CH_4, methane; C_2: C_2H_6, ethane; C_3: C_3H_8, propane; iC_4: *i*-sobutane; nC_4: *n*-butane; iC_5: *i*-sopentane; and nC_5: *n*-pentane.

reasonable parameter. Furthermore, the sample mass used for the HTD experiments was approximately 2.0 g, minimizing the impact of source rock heterogeneity on the results and enhancing the accuracy of the shale oil assessment.

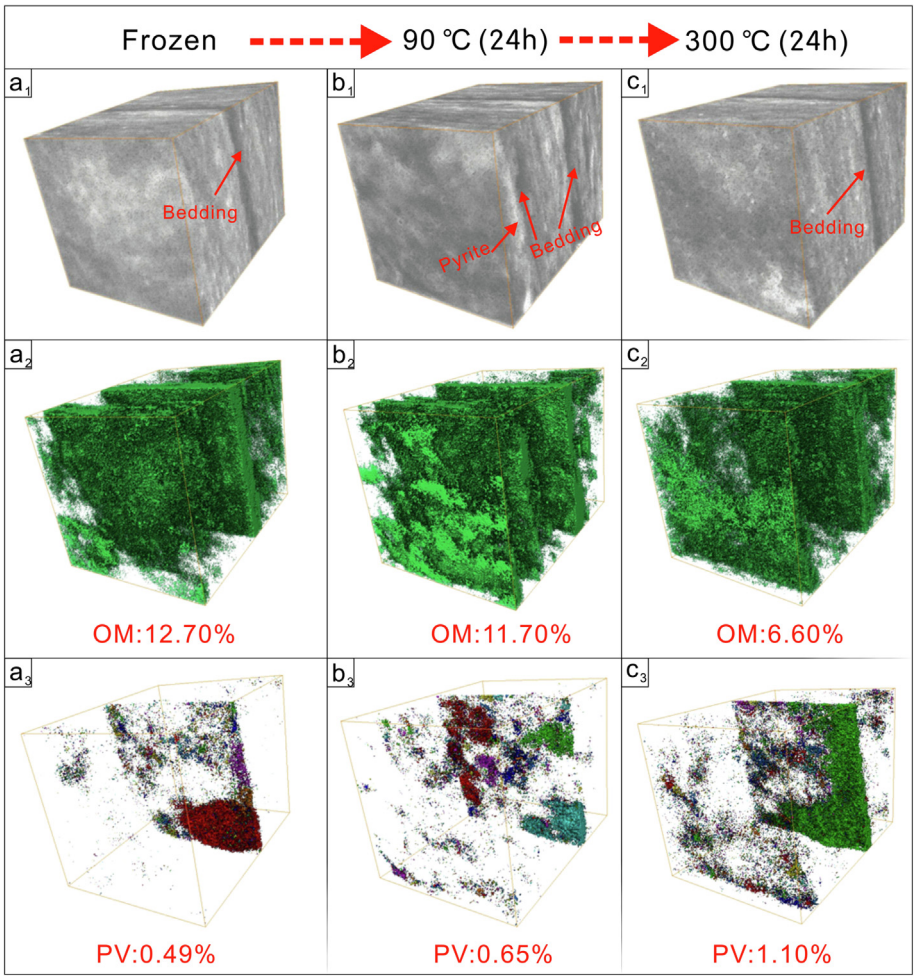

Fig. 8. Three-dimensional distributions of CT scans for shale sample S_{79} at different temperatures corresponding to three stages of HTD experiments (resolution: 3 μm). (a_1), (b_1) and (c_1): full view; (a_2), (b_2) and (c_2): the green areas represent organic matter (OM); and (a_3), (b_3) and (c_3): the different color areas represent different connected pore volumes (PVs), the same color represents a specific connected pore. (For interpretation of the references to color in this figure legend, the reader is referred to the web version of this article.)

5.2. The geochemical significance of restoring evaporative loss

5.2.1. The effect of evaporative loss on different TOC shale

In Fig. 11, the correlations between the percentage of S_g and S_0 contents in THC and TOC for all shale samples are shown. The study found that the percentage of evaporative loss on the conventional Rock-Eval S_1 peak, S_g and S_0, has a significant negative association with the TOC content. Even though the evaporative loss of S_g is below 10%, S_0′s fraction is higher than 10%, reaching 35.29%. As a result, the overall percentage of lost hydrocarbons could be as high as 42.6%. This discovery highlights the importance of timely organic geochemical core studies to accurately characterize and quantify the potential of shale and tight reservoir formations, especially for low TOC-poor source rocks. Failing to consider the extent of loss of S_g and S_0 could lead to a significant underestimation of potential shale oil contained in the target formation.

In many laboratories, the status of volatile light hydrocarbons in source rock samples is often overlooked during traditional Rock-Eval analysis and solvent extraction. This is because the storage conditions of the samples, including time-lapse and storage temperature after preparation, are not strictly regulated. It's crucial to store crushed samples in sealed vials or cloth/paper bags until instrumental analysis. Unattended samples can result in a substantial change in hydrocarbon concentrations, particularly for those reaching C_{10}, within just 21 h after preparation. Collection and storage of core and cuttings can also lead to significant evaporative loss of gaseous and light hydrocarbons (up to C_{10}) before instrumental analysis (Jiang et al., 2016). Hence, immediate well-site analyses are highly recommended. Alternatively, preservation methods such as deep freezing or aluminum foil wrapping followed by the waxing of the cores can minimize the loss of volatile components in the samples.

5.2.2. Effect of evaporative loss on shale oil classification and grading evaluation criteria

Determining the viable portion of shale hydrocarbon resources that can be exploited at present, as well as those that may become accessible in the near future as technology advances or remains out of reach despite further developments, is crucial. Shale oil deposits should ideally be classified based on their enrichment degree and commercial recoverability. Since enrichment is a crucial factor in determining recoverability, assessing it becomes the first step in evaluating and classifying shale oil. Shale oil can be classified into three levels: scattered (ineffective), low-efficiency, and enriched resources based on the oil and TOC contents of the source rock (Lu et al., 2012). TOC values corresponding to the two turning points of the upper envelope are the triple-division thresholds from the TOC point. The S_1* or THC value corresponding to the intersection of the upper envelope and TOC threshold (Threshold 1) are the oil content dividing point (Point 1) of ineffective and

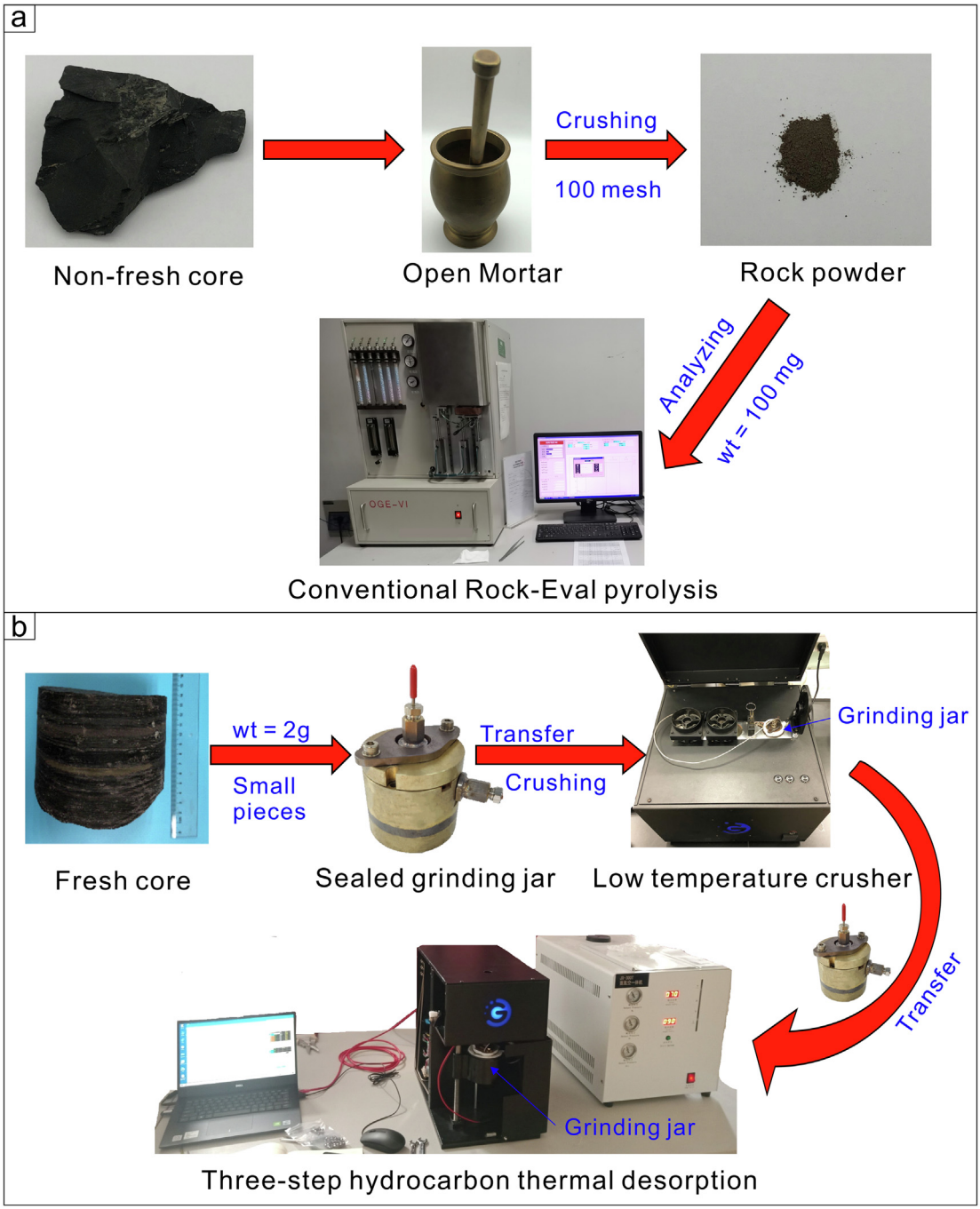

Fig. 9. Comparison of experimental procedures between (a) conventional Rock-Eval pyrolysis and (b) three-step hydrocarbon thermal desorption.

low-efficiency resources. The dividing point between low-efficiency and enriched resources (Threshold 2) can be defined as the oil content value corresponding to the stable section of the lower envelope or as the average of the oil content corresponding to the stable section of the upper envelope and the oil content corresponding to Threshold 1.

As seen in Fig. 12, the two TOC dividing points (Thresholds 1 and 2) of Chang 7 member shale oil can be defined as 2.0% and 8.0%, respectively. Moreover, whether the S_1* or THC value was chosen as the oil content parameter, the TOC value of these two triple-division limits remained the same. However, it was obvious that Thresholds 1 and 2 of the oil content were extremely different. In Fig. 12 (a), the oil contents corresponding to two triple-division limits were 4.0 mg/g and 12.0 mg/g. When gaseous and light hydrocarbons were considered, the two thresholds dramatically rose to 5.0 mg/g and 15.5 mg/g, respectively. Three zones were defined by combining the TOC and oil contents. The red area represents the ineffective resources, the blue area represents the low-efficiency resources, and the green area represents the enriched resources. Note that regardless of whether the triple-division limits changed as a result of more accurate oil contents, the area to which the shale samples belonged did not alter appreciably.

5.3. Evolution of pore volume during hydrocarbon thermal desorption experiment

The Hodot coal pore system is a widely used method for classifying shale reservoirs. It categorizes pores into four groups based

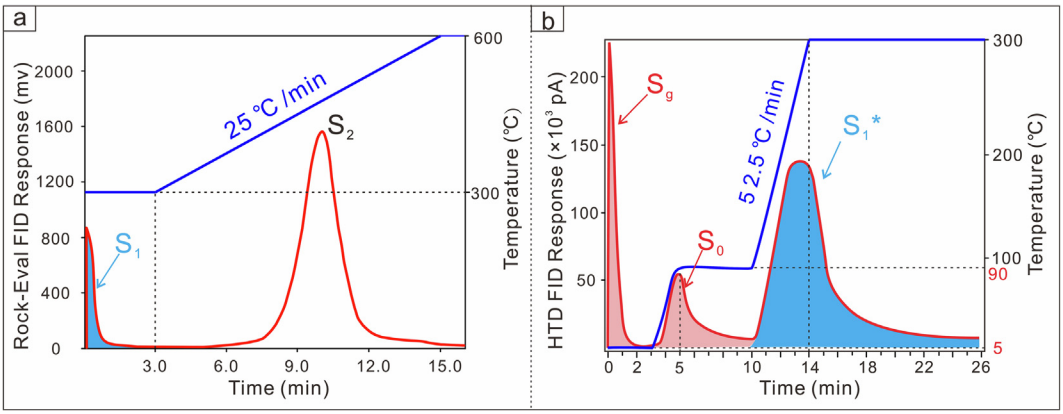

Fig. 10. Schematic of FID pyrograms showing the evolution of organic compounds from rock samples during heating. The red line is the real-time signal, and the blue line is the temperature curve. (a) conventional Rock-Eval pyrolysis and (b) three-step hydrocarbon thermal desorption. (For interpretation of the references to color in this figure legend, the reader is referred to the web version of this article.)

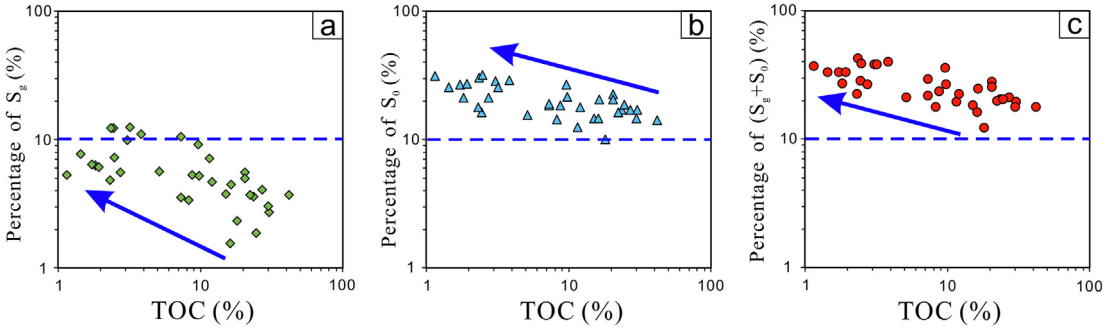

Fig. 11. Cross plot showing the percentage of S_g and S_0 contents and TOC for the Chang 7_3 submember shale.

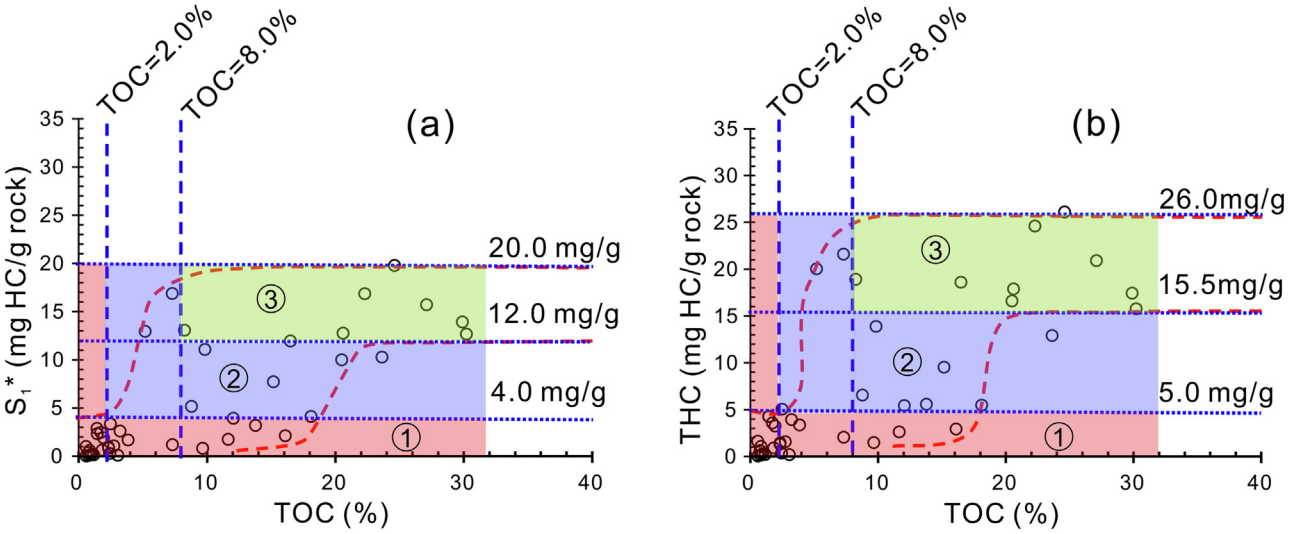

Fig. 12. TOC versus oil content of mature source rocks of the Chang 7 member. (a) The oil content was adopted as parameter S_1^* and (b) the oil content was adopted as parameter THC (THC = S_g + S_0 + S_1^*). ①: red area represents ineffective resources; ②: blue area represents low-efficiency resources; and ③: green area represents enriched resources. (For interpretation of the references to color in this figure legend, the reader is referred to the web version of this article.)

on their size: micropores (less than 10 nm), small pores (10–100 nm), medium pores (100–1000 nm), and large pores (greater than 1000 nm) (Li et al., 2016). Pyrolysis is a process that increases the porosity of oil shale and changes the size of its pores from primarily nano- to micronano-sized (Lei et al., 2021). During the high-temperature pyrolysis process, organic matter is converted to petroleum, while solid structures are thermally fractured. This creates a significant number of pores and fractures on both micro and macro scales, considerably improving shale pore structure (Saif et al., 2019). However, the thermal cracking and kerogen breakdown of macromolecular organic matter and certain inorganic minerals in oil shale to form tar typically occurs at temperatures

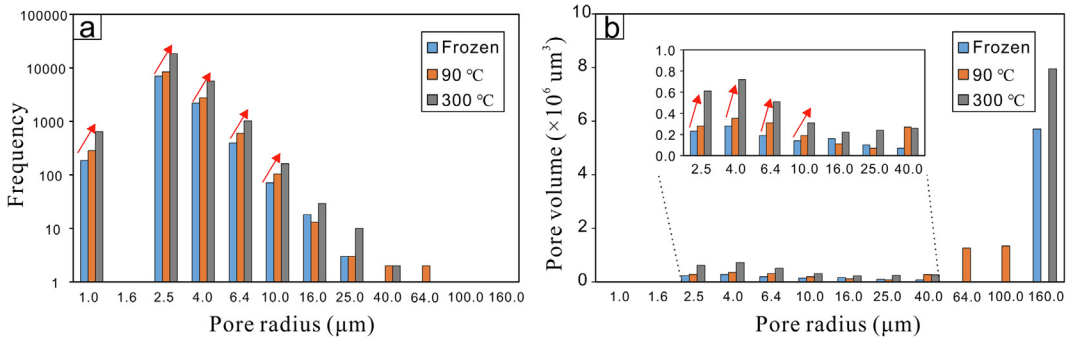

Fig. 13. Micro-CT scanning pore size distributions at three different temperature stages. (a) Statistics of different pore radii and (b) volume of pores with different radii.

ranging from 350 to 600 °C (Guo et al., 2020). Zhan et al. (Zhan et al., 2022) explained that at temperatures ranging from 200 °C to 410 °C, kerogen is first depolymerized into an asphalt monomer, which then decomposes into shale oil and gas as the temperature increases from 410 °C to 500 °C. In this study, the shale was heated to 300 °C using the HTD experiment temperature program, and real kerogen pyrolysis had not yet occurred. At 300 °C, Wei and Sheng (Wei and Sheng, 2022) found that the volumetric proportions of micropores and mesopores decreased, while the volumetric percentage of macropores significantly increased during the in situ heat treatment of Chang 7_3 shale. The researchers also discovered that preexisting natural fractures propagated on a small scale, and some new cracks were generated in situ in some areas, leading to an increase in both the number and length of cracks within shale at temperatures ranging from 100 to 300 °C. This phenomenon explains the increase in frequency and volume of shale cavities with various radii from the frozen state to 300 °C, as shown in Fig. 13.

6. Conclusions

(1) The Chang $7_{3\text{-}2}$ layer, which is alginate-rich mud shale, had undergone thermally developed and is located in the oil window. Most importantly, the majority of the TOC content is greater than 8.0 wt%, which is a strong indicator that this layer has a high potential for hydrocarbon generation.

(2) The proportion of S_g and S_0 had an opposite correlation with the TOC content, indicating that the loss of evaporation had a greater impact on the final shale oil content for lower-quality source rocks. S_g and S_0 were mainly made up of $C_{1\text{-}5}$ and $C_{1\text{-}7}$ hydrocarbons, respectively. $C_{1\text{-}3}$ gaseous hydrocarbons constituted a significant portion of S_g and S_0 (as much as 42.93%). On the other hand, the hydrocarbons observed in S_1* were primarily n-alkanes with relatively higher carbon numbers ranging from C_{16} to C_{31}.

(3) X-ray micro-CT scans offer a direct and precise view of the pore size distribution and changes in organic matter that occur as a result of shale heating. From the frozen state to 300 °C, the shale experiences a remarkable decrease in organic matter and a significant increase in pore volume. The most substantial modifications take place between 90 °C and 300 °C, with macropores and fractures being the primary contributors to the rise in pore volume.

(4) The shale oil triple-division limits were significantly affected by the loss of gaseous and light hydrocarbons through evaporation. To ensure accuracy, it is necessary to adjust these thresholds based on more precise oil content analyses. However, the resource zones, namely ineffective, low-efficient, and enriched resources, to which the samples belonged will remain unaltered.

CRediT authorship contribution statement

Gang Yan: Investigation, Writing – original draft, Visualization, Formal analysis. **Yao-Hui Xu:** Conceptualization, Writing – review & editing, Funding acquisition, Supervision. **Wang-Lin Xu:** Methodology, Project administration. **Bin Bai:** Project administration, Funding acquisition. **Ying Bai:** Methodology, Conceptualization. **Yun-Peng Fan:** Methodology, Data curation. **Shan-Shan Li:** Visualization. **Ming Zhong:** Writing – review & editing. **Yan Liu:** Methodology, Writing – review & editing. **Zhi-Yao Xu:** Methodology.

Declaration of Competing Interest

The authors declare that they have no known competing financial interests or personal relationships that could have appeared to influence the work reported in this paper.

Acknowledgments

This study is financially supported by the National Natural Science Foundation of China (Grant Number 41972122, 42172139 and 42072186), the China Scholarship Council (CSC), the Open Foundation of Cooperative Innovation Center of Unconventional Oil and Gas, Yangtze University (Ministry of Education & Hubei Province) (Grant Number UOGBX 2022-03) and PetroChina Innovation Found (No. 2020D-5007-0101). We thank Dr. Yong Ma (China University of Petroleum, Beijing) for his excellent technical assistance in the laboratory experiments involving X-ray micro-CT analysis and are grateful to two anonymous reviewers for their careful and constructive reviews of this paper.

Appendix A. Supplementary data

Supplementary data to this article can be found online at https://doi.org/10.1016/j.gsf.2023.101677.

References

Abrams, M.A., Dieckmann, V., Curiale, J.A., Clark, R., 2014. Hydrocarbon charge considerations in liquid-rich unconventional petroleum systems. American Association of Petroleum Geologists Search and Discovery Article.

Bohacs, K., Passey, Q., Rudnicki, M., Esch, W., Lazar, O., 2013. The spectrum of fine-grained reservoirs from'shale gas' to'shale oil'/tight liquids: essential attributes, key controls, practical characterization, IPTC 2013: International Petroleum Technology Conference. European Association of Geoscientists & Engineers, pp. cp-350-00187.

Budiman, H., Nuryatini, Zuas, O., 2015. Comparison between GC-TCD and GC-FID for the determination of propane in gas mixture. Procedia Chem. 16, 465-472. https://doi.org/10.1016/j.proche.2015.12.080.

Chen, J., Pang, X., Pang, H., Chen, Z., Jiang, C., 2018. Hydrocarbon evaporative loss evaluation of lacustrine shale oil based on mass balance method: Permian

Lucaogou Formation in Jimusaer Depression, Junggar Basin. Mar. Petrol. Geol. 91, 422–431. https://doi.org/10.1016/j.marpetgeo.2018.01.021.
Cooles, G., Mackenzie, A., Quigley, T., 1986. Calculation of petroleum masses generated and expelled from source rocks. Org. Geochem. 10, 235–245. https://doi.org/10.1016/0146-6380(86)90026-4.
Corso, J., Ruffell, A., Preto, N., 2018. The Carnian Pluvial Episode (Late Triassic): New insights into this important time of global environmental and biological change. J. Geol. Soc. 175 (6), 986–988. https://doi.org/10.1144/jgs2018-185.
Energy Information Administration (EIA). 2015. From: https://www.eia.gov/.
Fu, J., Li, S., Niu, X., Deng, X., Zhou, X., 2020. Geological characteristics and exploration of shale oil in Chang 7 member of Triassic Yanchang Formation, Ordos Basin. NW China. Petrol. Explora. Dev. 47 (5), 931–945. https://doi.org/10.1016/S1876-3804(20)60107-0.
Guo, W., Yang, Q., Sun, Y., Xu, S., Kang, S., Lai, C., Guo, M., 2020. Characteristics of low temperature co-current oxidizing pyrolysis of Huadian oil shale. J. Anal. Appl. Pyrol. 146, 104759. https://doi.org/10.1016/j.jaap.2019.104759.
Hou, L., Luo, X., Lin, S., Zhao, Z., Li, Y., 2021. Quantitative Measurement of Retained Oil in Organic-Rich Shale—A Case Study on the Chang 7 Member in the Ordos Basin. China. Front. Earth Sci. 9. https://doi.org/10.3389/feart.2021.662586.
Hou, H., Shao, L., Li, Y., Lu, J., Li, Z., Wang, S., Zhang, W., Wen, H., 2017. Geochemistry, reservoir characterization and hydrocarbon generation potential of lacustrine shales: A case of YQ-1 well in the Yuqia Coalfield, northern Qaidam Basin, NW China. Mar. Petrol. Geol. 88, 458–471. https://doi.org/10.1016/j.marpetgeo.2017.08.030.
Hunt, J., Huc, A., Whelan, J., 1980. Generation of light hydrocarbons in sedimentary rocks. Nature 288, 688–690. https://doi.org/10.1038/288688a0.
Jarvie, D.M., Hill, R.J., Ruble, T.E., Pollastro, R.M., 2007. Unconventional shale-gas systems: The Mississippian Barnett Shale of north-central Texas as one model for thermogenic shale-gas assessment. Aapg. Bull. 91, 475–499. https://doi.org/10.1306/12190606068.
Jarvie, D.M., 2012. Shale resource systems for oil and gas: part2-shale-oil resource systems. In: Shale reservoirs: giant resources for the 21st century. https://doi.org/10.1306/13321447M973489.
Jiang, Q., Li, M., Qian, M., Li, Z., Li, Z., Huang, Z., Zhang, C., Ma, Y., 2016. Quantitative characterization of shale oil in different occurrence states and its application. Petrol. Geol. Exp. 38 (6), 842–849 https://doi.org/10.11781/sysydz201606842.
Jiang, C., Mort, A., Sanei, H., Chen, Z., Milovic, M., Robinson, R., 2015. S_1 peak of Rock-Eval analysis: What does it represent for unconventional hydrocarbon resource assessment, GeoConvention: New Horizons, May 4–8, Calgary, 2015. Alberta, Canada.
Jiang, C., Chen, Z., Mort, A., Milovic, M., Robinson, R., Stewart, R., Lavoie, D., 2016. Hydrocarbon evaporative loss from shale core samples as revealed by Rock-Eval and thermal desorption-gas chromatography analysis: Its geochemical and geological implications. Mar. Petrol. Geol. 70, 294–303. https://doi.org/10.1016/j.marpetgeo.2015.11.021.
Jin, Z.J., Bai, Z.R., Gao, B., Li, M., 2019. Has China ushered in the shale oil and gas revolution. Oil Gas Geol. 40, 451–458 http://ogg.pepris.com/EN/10.11743/ogg20190301.
Khan, I., Zhong, N., Luo, Q., Ai, J., Yao, L., Luo, P., 2020. Maceral composition and origin of organic matter input in Neoproterozoic-Lower Cambrian organic-rich shales of Salt Range Formation, upper Indus Basin. Pakistan. Int. J. Coal Geol. 217, 103319. https://doi.org/10.1016/j.coal.2019.103319.
Kuang, L., Hou, L., Wu, S., Cui, J., Tian, H., Zhang, L., Zhao, Z., Luo, X., Jiang, X., 2022. Organic matter occurrence and pore-forming mechanisms in lacustrine shales in China. Petrol. Sci. 19 (4), 1460–1472. https://doi.org/10.1016/j.petsci.2022.03.005.
Lei, J., Pan, B., Guo, Y., Fan, Y., Xue, L., Deng, S., Zhang, L., Ruhan, A., 2021. A comprehensive analysis of the pyrolysis effects on oil shale pore structures at multiscale using different measurement methods. Energy 227, 120359. https://doi.org/10.1016/j.energy.2021.120359.
Li, A., Ding, W., He, J., Dai, P., Yin, S., Xie, F., 2016. Investigation of pore structure and fractal characteristics of organic-rich shale reservoirs: A case study of Lower Cambrian Qiongzhusi formation in Malong block of eastern Yunnan Province, South China. Mar. Petrol. Geol. 70, 46–57. https://doi.org/10.1016/j.marpetgeo.2015.11.004.
Li, J., Wang, M., Chen, Z., Lu, S., Jiang, C., Chen, G., Tian, S., 2019. Evaluating the total oil yield using a single routine Rock-Eval experiment on as-received shales. J. Anal. Appl. Pyrol. 144, 104707. https://doi.org/10.1016/j.jaap.2019.104707.
Li, J., Jiang, C., Wang, M., Xu, L., Li, M., Yu, C., Wu, Y., Lu, S., 2022. Determination of in situ hydrocarbon contents in shale oil plays. Part 1: Is routine Rock-Eval analysis reliable for quantifying the hydrocarbon contents of preserved shale cores? Org. Geochem. 170, 104449. https://doi.org/10.1016/j.orggeochem.2022.104449.
Li, W., Lu, S., Xue, H., Zhang, P., Hu, Y., 2015. Oil content in argillaceous dolomite from the Jianghan Basin, China: Application of new grading evaluation criteria to study shale oil potential. Fuel 143, 424–429. https://doi.org/10.1016/j.fuel.2014.11.080.
Lin, M., Xi, K., Cao, Y., Zhu, R., Niu, X., Xin, H., Ma, W., 2023. Cyclicity related to solar activity in lacustrine organic-rich shales and their significance to shale-oil reservoir formation. Geosci. Front. 14 (5), 101586. https://doi.org/10.1016/j.gsf.2023.101586.
Liu, X., Li, S., Guo, Q., Zhou, X., Liu, J., 2021. Characteristics of rock types and exploration significance of the shale strata in the Chang 73 sub-member of Yanchang Formation, Ordos Basin. China. J. Nat. Gas Geosci. 6 (6), 363–373. https://doi.org/10.1016/j.jnggs.2021.12.003.
Liu, D., Su, J., Gu, Z., Qi, Y., Yang, F., Tian, T., Ye, F., Zhan, S., 2021. Geochemical Properties and Pore Structure Control on Oil Extraction of Shale. Lithosphere-Us 2021. https://doi.org/10.2113/2021/6646791.
Liu, C., Wang, Z., Guo, Z., Hong, W., Dun, C., Zhang, X., Li, B., Wu, L., 2017. Enrichment and distribution of shale oil in the Cretaceous Qingshankou Formation, Songliao Basin, northeast China. Mar. Petrol. Geol. 86, 751–770. https://doi.org/10.1016/j.marpetgeo.2017.06.034.
Liu, Y., Zeng, J., Yang, G., Jia, W., Liu, S., Kong, X., Li, S., 2021. An innovative method for the characterization of oil content in lacustrine shale-oil systems: A case study from the Middle Permian Lucaogou Formation in the Jimusaer Sag. Junggar Basin. Mar. Petrol. Geol. 130. https://doi.org/10.1016/j.marpetgeo.2021.105112.
Lu, S., Huang, W., Chen, F., Li, J., Wang, M., Xue, H., Wang, W., Cai, X., 2012. Classification and evaluation criteria of shale oil and gas resources: Discussion and application. Petrol. Explor. Dev. 39, 268–276. https://doi.org/10.1016/s1876-3804(12)60042-1.
Peters, K., 1986. Guidelines for evaluating petroleum source rock using programmed pyrolysis. Aapg. Bull. 70, 318–329. https://doi.org/10.1306/94885688-1704-11d7-8645000102c1865d.
Pickel, W., Kus, J., Flores, D., Kalaitzidis, S., Christanis, K., Cardott, B., Misz-Kennan, M., Rodrigues, S., Hentschel, A., Hamor-Vido, M., 2017. Classification of liptinite–ICCP System 1994. Int. J. Coal Geol. 169, 40–61. https://doi.org/10.1016/j.coal.2016.11.004.
Preto, N., Kustatscher, E., Wignall, P., 2010. Triassic climates—state of the art and perspectives. Palaeogeogr. Palaeocl. Palaeoecol. 290 (1–4), 1–10. https://doi.org/10.1016/j.palaeo.2010.03.015.
Pu, X., Zhou, L., Han, W., Zhou, J., Wang, W., Wei, Z., Chen, S., Shi, Z., Liu, S., 2016. Geologic features of fine-grained facies sedimentation and tight oil exploration: A case from the second Member of Paleogene Kongdian Formation of Cangdong sag, Bohai Bay Basin. Petrol. Explor. Dev. 43, 26–35. https://doi.org/10.1016/s1876-3804(16)30003-9.
Romero-Sarmiento, M.F., 2019. A quick analytical approach to estimate both free versus sorbed hydrocarbon contents in liquid-rich source rocks. AAPG Bull. 103 (9), 2031–2043. https://doi.org/10.1306/02151918152.
Saif, T., Lin, Q., Singh, K., Bijeljic, B., Blunt, M.J., 2016. Dynamic imaging of oil shale pyrolysis using synchrotron X-ray microtomography. Geophys. Res. Lett. 43, 6799–6807. https://doi.org/10.1002/2016gl069279.
Saif, T., Lin, Q., Gao, Y., Al-Khulaifi, Y., Marone, F., Hollis, D., Blunt, M.J., Bijeljic, B., 2019. 4D in situ synchrotron X-ray tomographic microscopy and laser-based heating study of oil shale pyrolysis. Appl. Energ. 235, 1468–1475. https://doi.org/10.1016/j.apenergy.2018.11.044.
Sun, H., Cai, X., Zhou, D., Gao, B., Zhao, P., 2019. Practice and prospect of Sinopec shale oil exploration. China Petrol. Explor. 24, 569. https://doi.org/10.3969/j.issn.1672-7703.2019.05.004.
Tang, Y., Cao, J., He, W., Guo, X., Zhao, K., Li, W., 2021. Discovery of shale oil in alkaline lacustrine basins: the Late Paleozoic Fengcheng Formation, Mahu Sag, Junggar Basin. China. Petrol. Sci. 18 (5), 1281–1293. https://doi.org/10.1016/j.petsci.2021.04.001.
Wang, E., Li, C., Feng, Y., Song, Y., Guo, T., Li, M., Chen, Z., 2022. Novel method for determining the oil moveable threshold and an innovative model for evaluating the oil content in shales. Energy 239. https://doi.org/10.1016/j.energy.2021.121848.
Wang, M., Tian, S., Chen, G., Xue, H., Huang, A., Wang, W., 2014. Correction method of light hydrocarbons losing and heavy hydrocarbon handling for residual hydrocarbon (S_1) from shale. Acta Geol. Sin-Engl. 88 (6), 1792–1797. https://doi.org/10.1111/1755-6724.12345.
Wang, M., Wilkins, R.W., Song, G., Zhang, L., Xu, X., Li, Z., Chen, G., 2015. Geochemical and geological characteristics of the Es_3^L lacustrine shale in the Bonan sag, Bohai Bay Basin. China. Int. J. Coal Geol. 138, 16–29. https://doi.org/10.1016/j.coal.2014.12.007.
Wang, M., Guo, Z., Jiao, C., Lu, S., Li, J., Xue, H., Li, J., Li, J., Chen, G., 2019. Exploration progress and geochemical features of lacustrine shale oils in China. J. Petrol. Sci. Eng. 178, 975–986. https://doi.org/10.1016/j.petrol.2019.04.029.
Wang, M., Li, M., Li, J., Xu, L., Zhang, J., Zhang, J., 2022. The key parameter of shale oil resource evaluation: Oil content. Petrol. Sci. 19 (4), 1443–1459. https://doi.org/10.1016/j.petsci.2022.03.006.
Wei, Z., Sheng, J., 2022. Changes of pore structures and permeability of the Chang 7_3 medium-to-low maturity shale during in-situ heating treatment. Energy 248, 123609. https://doi.org/10.1016/j.energy.2022.123609.
Wright, M.C., Court, R.W., Kafantaris, F.-C.-A., Spathopoulos, F., Sephton, M.A., 2015. A new rapid method for shale oil and shale gas assessment. Fuel 153, 231–239. https://doi.org/10.1016/j.fuel.2015.02.089.
Xie, X., Li, M., Xu, J., Snowdon, L.R., Volkman, J.K., 2020. Geochemical characterization and artificial thermal maturation of kerogen density fractions from the Eocene Huadian oil shale. NE China. Org. Geochem. 144, 103947. https://doi.org/10.1016/j.orggeochem.2019.103947.
Yang, M., Liu, C., Zheng, M., Lan, C., Tang, X., 2007. Sequence framework of two different kinds of margins and their response to tectonic activity during the Middle-Late Triassic, Ordos Basin. Sci. China Ser. D: Earth Sci. 50, 203–216. https://doi.org/10.1007/s11430-007-6017-y.
Yang, H., Niu, X., Xu, L., Feng, S., You, Y., Liang, X., Wang, F., Zhang, D., 2016. Exploration potential of shale oil in Chang7 Member, Upper Triassic Yanchang Formation, Ordos Basin, NW China. Petrol. Explor. Dev. 43, 560–569. https://doi.org/10.1016/s1876-3804(16)30066-0.
Yang, H., Zhang, W., 2005. Leading effect of the seventh member high-quality source rock of Yanchang Formation in Ordos Basin during the enrichment of low-

penetrating oil-gas accumulation: Geology and geochemistry. Geochimica 34, 147–154 https://doi.org/10.19700/j.0379-1726.2005.02.007.

Zhan, H., Qin, F., Chen, S., Chen, R., Meng, Z., Miao, X., Zhao, K., 2022. Two-step pyrolysis degradation mechanism of oil shale through comprehensive analysis of pyrolysis semi-cokes and pyrolytic gases. Energy 241, 122871. https://doi.org/10.1016/j.energy.2021.122871.

Zhang, L., Li, J., Li, Z., Jarvie, D., Hill, R., Ruble, T., Pollastro, R., 2012. Continental basin in the key geological problems of shale oil exploration and development–a case study of Dongying sag. Oil Shale Resources and Exploration and Development Technology International Symposium.

Zhang, W., Xie, L., Yang, W., Qin, Y., 2017. Micro fractures and pores in lacustrine shales of the upper Triassic Yanchang Chang7 Member, Ordos Basin. China. J. Petrol. Sci. Eng. 156, 194–201. https://doi.org/10.1016/j.petrol.2017.03.044.

Zhao, X., Zhou, L., Pu, X., Han, W., Jin, F., Xiao, D., Shi, Z., Deng, Y., Zhang, W., Jiang, W., 2019. Exploration breakthroughs and geological characteristics of continental shale oil: A case study of the Kongdian Formation in the Cangdong Sag. China. Mar. Petrol. Geol. 102, 544–556. https://doi.org/10.1016/j.marpetgeo.2018.12.020.

Zhu, R., Zou, C., Wu, S., Yang, Z., Mao, Z., Yang, H., Fan, C., Hui, X., Cui, J., Su, L., 2019. Mechanism for generation and accumulation of continental tight oil in China. Oil Gas Geol. 40, 1168–1184 http://ogg.pepris.com/EN/10.11743/ogg20190602.